Available online at www.sciencedirect.com

ScienceDirect

Journal of the European Ceramic Society 30 (2010) 1359–1372

www.elsevier.com/locate/jeurceramsoc

Microstructure and mechanical properties of Al_2O_3 matrix nanocomposites produced by solid state precipitation

Amartya Mukhopadhyay, Richard I. Todd *

Department of Materials, University of Oxford, Oxford OX1 3PH, UK

Received 30 October 2009; received in revised form 26 November 2009; accepted 1 December 2009
Available online 12 January 2010

Abstract

A novel and economical processing route for the production of Al_2O_3-based ceramic nanocomposites via solid solution–precipitation is reported. Dense (>98% ρ_{th}) and homogeneous solid solutions of 10 wt.% Fe_2O_3 in Al_2O_3 were produced by pressureless sintering at 1450 °C in air. Aging of the solid solutions in a reducing atmosphere at temperatures in the range 1250–1550 °C for different durations (up to 50 h) resulted in the precipitation of $FeAl_2O_4$ as second phase particles throughout the bulk of the samples. The optimum aging schedule resulted in a final microstructure comprising nano-sized (~100 nm) intragranular $FeAl_2O_4$ particles, along with coarser micro-sized particles on the matrix grain boundaries and triple point corners. Additionally, surface layers containing metallic Fe and with thicknesses up to ~100 µm were formed due to the further reduction of $FeAl_2O_4$. After removal of this surface layer, the hybrid nano/microcomposites possessed improved fracture toughness (by ~40%) and flexural strength (by ~50%) with respect to monolithic Al_2O_3.

Keywords: Nanocomposite; Aging; Microstructure; Mechanical properties

1. Introduction

The mechanical and tribological properties of one of the technologically most important structural ceramics, alumina (Al_2O_3), can be significantly improved by the incorporation of nano-sized secondary phase particles.[1–11] In particular, it has been established that the incorporation of nanocrystalline SiC in an alumina matrix can result in an improvement of strength by ~20% or more and of the resistance to severe wear by a factor of ~3.[1,4,7–9,12] In addition to the extensive research on Al_2O_3–SiC nanocomposites, other nanocomposites based on alumina, such as Al_2O_3–TiC,[10] Al_2O_3–TiCN–SiC,[11] have also been developed with all showing improved properties with respect to monolithic alumina. However, in spite of being such promising materials, ceramic nanocomposites have not yet penetrated the commercial market.

One of the major hindrances to the commercial application of ceramic nanocomposites arises from the challenges encountered during processing. To date, most nanocomposites have been made via conventional powder processing routes, which involve the mixing of nano-sized starting powders, followed by sintering. However, the incorporation of refractory, non-oxide second phase nanoparticles, such as SiC, severely inhibits densification to the extent that the attainment of near theoretical sinter densities via pressureless sintering is possible only with small amounts of SiC and very high temperatures.[1,9,12] Although Y_2O_3 has proved to be a viable sintering aid to achieve densification of Al_2O_3–SiC nanocomposites via pressureless sintering,[12] only modest lowering of sintering temperature has been possible and only for a very narrow composition-processing window for nanocomposites containing not more than 5 vol.% SiC. On the other hand, the use of less refractory oxide second phases alleviates the sintering problem but leads to severe coarsening so that the essential nano-structure is lost if sintered using conventional pressureless sintering.[1] These problems make it necessary to use hot pressing or spark plasma sintering for developing ceramic nanocomposites containing moderate amounts of nano-sized second phase particles.[1] However, such techniques possess serious drawbacks with respect to mass scale commercial production in the sense that, as well as being very expensive, they are not suitable for continuous batch production and severely limit the shape and size of the components that can be produced. A further problem with the use of non-oxide particles is the possibility of oxidation during use at high temperature

---

* Corresponding author. Tel.: +44 1865 273718; fax: +44 1865 273783.
E-mail address: richard.todd@materials.ox.ac.uk (R.I. Todd).

0955-2219/$ – see front matter © 2009 Elsevier Ltd. All rights reserved.
doi:10.1016/j.jeurceramsoc.2009.12.007

and the consequent loss of the beneficial effects of the nanoparticles. Hence, in order to stimulate commercial application of alumina matrix nanocomposites, it is imperative to develop ceramic nanocomposites consisting only of oxide phases that can be produced using cheaper and more versatile processing techniques, which are suitable for commercial mass production.

One of the possible routes to develop ceramic nanocomposites is the in situ formation of nano-sized particles by precipitation during aging of supersaturated solid solutions. However, to date there are very few literature reports which explore the possibility of development of Al_2O_3-based oxide–oxide ceramic nanocomposites via such precipitation techniques. One of the earliest indications of precipitation from supersaturated solid solution in Al_2O_3 ceramics is the needle shaped precipitates (possibly TiO_2) observed in star sapphire.[13,14] However, the needles formed in such star sapphires are usually hundreds of micrometers in length. Submicron-sized TiO_2 needles within the matrix grains of polycrystalline Al_2O_3, along with coarser Al_2TiO_5 precipitates at the triple point corners of the matrix grain boundaries, were also obtained during heating in an oxidizing atmosphere of $(Al_{1-x},Ti_x^{3+})_2O_3$ solid solutions containing a maximum of only 0.6 cation% Ti.[15] In a more recent investigation, Wang et al.[6] developed an Al_2O_3-based nanocomposite by precipitation of nanocrystalline magnesium aluminium spinel ($MgAl_2O_4$) during aging in a reducing atmosphere of a supersaturated charge compensated solid solution of Mg^{2+} and Ti^{4+} ions in Al_2O_3. However, due to limited solubility in Al_2O_3, only a maximum of 2 mol% ($MgO + TiO_2$) can be incorporated during solution treatment which limits the volume fraction of the second phase particles that can be precipitated out during the aging treatment.

The present work reports the development of a novel and commercially feasible processing route based on solution/precipitation of nano-sized oxide particles by incorporating Fe^{3+} in Al_2O_3. Fe_2O_3 (haematite) has the same crystal structure as α-Al_2O_3 (corundum) and possesses substantial solubility in Al_2O_3 at moderately high temperatures in air (∼15 wt.% at ∼1410 °C).[16] Furthermore, under reducing conditions Fe^{3+} (of dissolved Fe_2O_3) can be reduced to Fe^{2+}, which being aliovalent to Al^{3+} possesses very limited solubility in Al_2O_3. Hence, it is expected that aging of Al_2O_3–Fe_2O_3 solid solutions under reducing conditions should lead to the formation of Fe^{2+}-containing precipitate particles. This work aims to examine the extent to which a uniform dispersion of nano-sized particles can be produced by optimising the processing conditions. It must be mentioned here that, although high purity nano-sized Al_2O_3 powders and ethanol as the dispersing medium have been used in the present work for aiding scientific study, such work can be carried out industrially using coarser, less pure commercial grades of powders and water as the dispersing medium.

2. Experimental procedure

2.1. Precursors and processing scheme

High purity (∼99.995%), fine (particle size ∼200 nm) α-Al_2O_3 powders (AKP50, Sumitomo, Japan) were used as the starting material for the matrix (Al_2O_3). In order to prevent abnormal grain growth during sintering and to enable near theoretical densification, the Al_2O_3 powders were doped with 250 ppm of MgO using pure MgO powders (99.95%; 120 nm; UBE, Japan).[17] The MgO doped Al_2O_3 powders were dispersed in ethanol using an ultrasonic probe. The incorporation of Fe^{3+} was achieved by adding a solution of $Fe(NO_3)_3.9H_2O$ (Sigma–Aldrich, UK, purity >98%) in ethanol to the alumina slurries. The $Fe(NO_3)_3$ solutions contained the requisite amount of the salt that would result in doping levels corresponding to 10 wt.% Fe_2O_3 in Al_2O_3. Some pure alumina slurries were also made for comparison. All the slurries were ball milled for 24 h in bottles made of polyethylene, using high purity (99.99%) alumina balls. After ball milling, the slurries were dried on a hot plate with constant stirring, using a magnetic stirrer, to prevent segregation. The dried powders were lightly crushed to remove agglomerates, gently ground in an Al_2O_3 mortar and pestle and passed through a 150 μm sieve.

Green compacts were produced by uniaxial cold pressing of the powders into 20 mm discs at 100 MPa. The first step in the present processing scheme involved sintering to near theoretical densities for the pure Al_2O_3 and Fe-containing Al_2O_3 pellets. The green compacts were densified using pressureless sintering in air inside an alumina tube furnace (Lenton, UK). The as-sintered pellets were around 3 mm thick. The Al_2O_3 samples containing 10 wt.% Fe_2O_3 will henceforth be referred to as 'A10F'. During the sintering cycle, the A10F green pellets were slowly heated (at 5 °C/min) up to a temperature of 750 °C and held there for 1 h in order to decompose the ferric nitrate to Fe_2O_3. Following this, a heating rate of 10 °C/min was used up to the sintering temperature of 1450 °C. The pure Al_2O_3 pellets were directly heated to the sintering temperature of 1450 °C from room temperature at a heating rate of 10 °C/min. The selected sintering temperature of 1450 °C corresponds to the temperature on the Al_2O_3–Fe_2O_3 phase diagram where ∼15 wt.% Fe_2O_3 is soluble in Al_2O_3.[16] Hence it is expected that all of the Fe_2O_3 in the A10F specimens will be dissolved in the Al_2O_3 during sintering to yield an alumina-based solid solution containing Fe^{3+} cations. In this perspective, the sintering step is designed to fulfil the dual purpose of attaining densification and developing Al_2O_3–10 wt.% Fe_2O_3 (A10F) solid solutions. To ensure complete dissolution and homogeneous distribution of Fe^{3+} in the cation sub-lattice of Al_2O_3, the samples were held at the sintering temperature (1450 °C) for 5 h (solution treatment). After completion of the solution treatment, in order to avoid the possible precipitation of Fe_2O_3 during furnace cooling, the samples were 'quenched' by pushing them immediately to the end of the furnace tube using an alumina rod, where the temperature is expected to be ∼100 °C.

The second major step in the heat treatment scheme was the generation of Fe-containing second phase particles during heat treatment of the densified Al_2O_3–10 wt.% Fe_2O_3 solid solutions. The supersaturated solid solutions were aged under reducing conditions using a N_2–4% H_2 forming gas mixture at different temperatures (1250–1550 °C) and for different durations up to 50 h.

2.2. Characterisation

The sintered densities of all the samples were measured in distilled water according to Archimedes' principle. For phase identification and microstructural characterization, the samples were ground and polished using 25, 6, 3, 1 and 0.25 μm diamond slurries in order to remove the external surfaces and produce optically reflective ceramographic surfaces representative of the sample cores. Furthermore, the samples were also cut along a diameter and polished to observe the microstructural development along the cross-sections.

The phase identification of the green pellets, sintered samples and aged samples was performed by X-ray diffraction (XRD) using CuKα radiation (Philips, Netherlands) at a collection rate of 3°/min. The change in interplanar spacing of the matrix due to solution and aging treatments was estimated from the shifts of the (1 1 3) and (2 2 6) Al_2O_3 peak positions in the XRD patterns. An extrapolation procedure[18] was used to obtain accurate values of interplanar spacings by plotting the calculated values of $d_{1\,1\,3}$ for each peak against $\cos^2\theta/\sin\theta$ and extrapolating the lines joining the points to $\cos^2\theta/\sin\theta = 0$.

In order to reveal the grain boundaries of the as-sintered pure Al_2O_3 and A10F solid solution samples, thermal etching was done at a temperature of 1400 °C for 15 min in air. Following thermal etching, the samples were again 'quenched' in the manner described earlier. The microstructures of all the polished surfaces were observed using a field emission scanning electron microscope (JEOL 6500F) operated at 20 kV. Elemental analysis was performed using EDS, attached to the SEM. Volume fractions of the second phase particles were determined via point counting on back scattered electron (BSE) images and the average particle sizes were determined from the mean of the major and minor axes of at least 20 particles, multiplied by 1.27 to obtain equivalent spherical diameters.[4] Sample preparation for transmission electron microscope (TEM) observations involved mechanical thinning of 3 mm discs, followed by ion-milling to electron transparency in a Gatan Duo Mill (5 kV). Observations were performed using a 200 kV JEOL 2000FX TEM, equipped with an EDS system.

The hardness of the composites/nanocomposites developed under optimum aging conditions, along with those of monolithic Al_2O_3, was measured by Vickers indentation (H_v) on polished surfaces with an indentation load of 5 kg and loading time 15s. Flexural strengths were measured using plain rectangular cross-section beams tested in four-point bending. The more conventional SEVNB method has been used to estimate the bulk fracture toughness of the nanocomposites and monolithic Al_2O_3. For the flexural strength and fracture toughness measurements, as-cut beams were polished on both long faces containing the loading axis and one long face normal to the loading axis using 25, 6, 3 and 1 μm diamond slurries. The final specimen dimensions were 13 mm × 2 mm × 2.5 mm. For SEVNB, the ratios between the notch depths and specimen thickness were between 0.2 and 0.3. The notches were sharpened by razor blade using diamond paste grades down to 1 μm so that the tip radii of the notches were less than ∼10 μm. The flexural strengths and fracture toughnesses were measured in the four-point bending configuration, using a crosshead loading rate of 5 N/min and inner and outer spans of 5.8 and 10 mm, respectively. The tests were performed on a universal testing machine (Dension-Mayes, U.K.). For estimating the fracture toughness, the following relation was used[19]:

$$K_{1C} = \frac{P_f(L_o - L_i)}{BW^{3/2}} \frac{3\alpha^{1/2}}{2(1-\alpha)^{3/2}} f(\alpha) \tag{1}$$

$$f(\alpha) = 1.9887 - 1.326\alpha - \frac{\alpha(1-\alpha)(3.49 - 0.68\alpha + 1.35\alpha^2)}{(1+\alpha)^2} \tag{2}$$

where P_f, L_o, L_i, B, W are experimentally measured fracture load, outer span, inner span, specimen width, and specimen depth, respectively. The pre-crack size (notch depth) enters the equation through α, where $\alpha = a/W$. The reported values are the averages of at least 5 independent measurements.

3. Results

3.1. Phase evolution

XRD patterns corresponding to the cores of the as-sintered pure Al_2O_3, calcined A10F pellets, solution treated A10F and aged (1450 °C; 0–50 h; $N_2 + 4\%\ H_2$ atmosphere) A10F are presented in Fig. 1a and b. Pattern 2 of Fig. 1a reveals that after calcination at 750 °C for 1 h, the $Fe(NO_3)_3{\cdot}9H_2O$ precursor has decomposed to α-Fe_2O_3, which is present as a secondary phase along with α-Al_2O_3 in the as-calcined pellets. In contrast, the XRD pattern corresponding to the as-sintered A10F (pattern 3) contains only peaks corresponding to α-Al_2O_3 revealing that the Fe_2O_3 (∼10 wt.%) has completely dissolved in the Al_2O_3 matrix during holding at the sintering temperature of 1450 °C, as is suggested by the Al_2O_3–Fe_2O_3 phase diagram.[16] The magnified view of the {1 0 4} peak of α-Al_2O_3 (Fig. 1b) shows a notable shift in the peak position towards the lower angle (2θ)/higher d-spacing side after solution treatment of A10F (compare patterns 1 and 3). Since the ionic radius of Fe^{3+} (0.065 nm) is larger than that of Al^{3+} (0.054 nm), dissolution of Fe^{3+} by substitution for Al^{3+} in the cationic sub-lattice of Al_2O_3[20] leads to the expansion of the lattice, as observed. Patterns 4–6 in Fig. 1a show the appearance of peaks corresponding to $FeAl_2O_4$ (iron aluminate spinel) on aging of solution treated A10F in the reducing atmosphere ($N_2 + H_2$ gas mixture). At the same time, peaks corresponding to α-Al_2O_3 get shifted back towards higher Bragg angles/lower d-spacing on reduction aging of the solid solutions (compare patterns 3 and 4 in Fig. 1b) as the Fe^{3+} comes out of solution with precipitation of $FeAl_2O_4$.

Insight into the effects of aging temperature and time on the progress of the precipitation reaction can be obtained by estimating the decrease in the interplanar spacing of the matrix (Al_2O_3) with respect to the solution treated A10F, caused by the diminution of Fe^{3+} from the solid solution. A plot showing the variations of the changes in Al_2O_3 interplanar spacing with aging duration at the different aging temperatures (1250, 1350, 1450 and 1550 °C) is presented in Fig. 1c. It can be observed

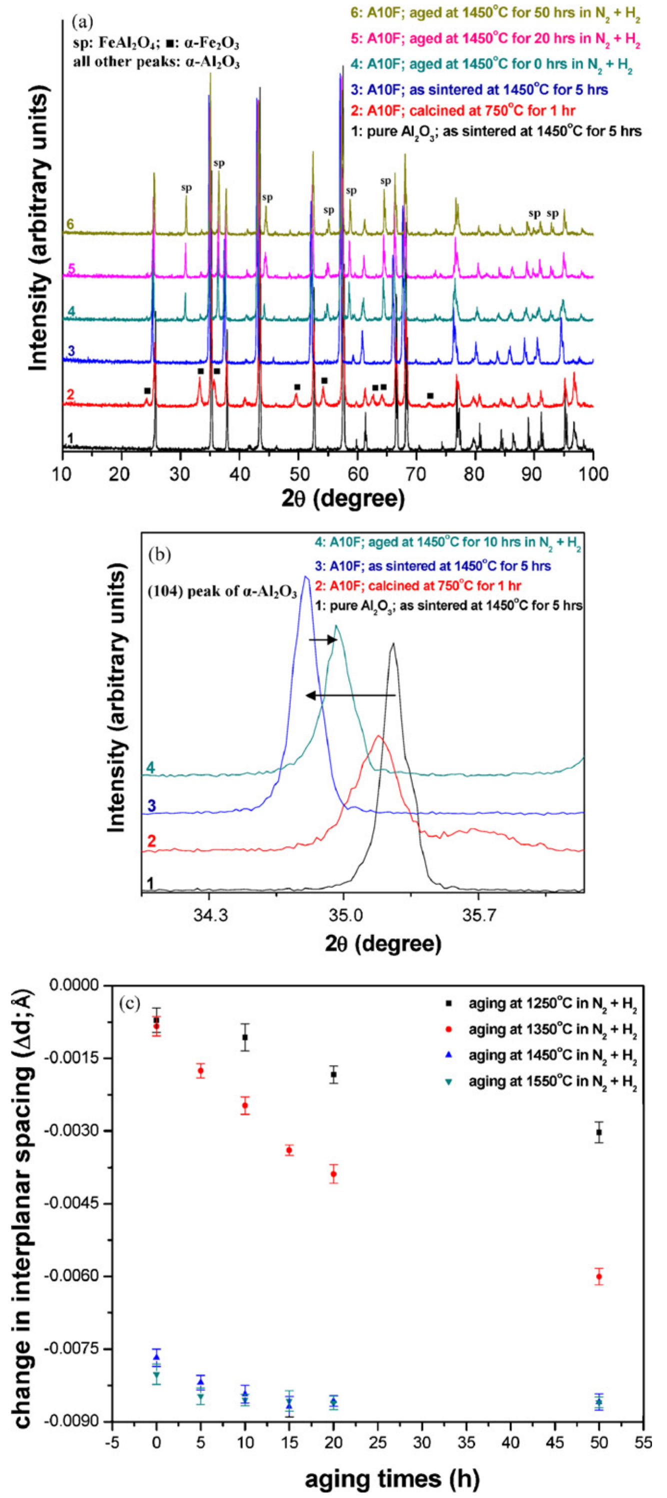

Fig. 1. (a) XRD patterns obtained from calcined A10F pellets and polished surfaces of as-sintered pure Al_2O_3 and A10F as solution treated and after subsequent aging at 1450 °C for 0, 20 and 50 h in reducing atmosphere ($N_2 + 4\%$ H_2 gas mixture). Note the appearance of spinel phase on aging of the supersaturated A10F solid solution; (b) magnified view of the {1 0 4} peak of α-Al_2O_3 showing peak shifts after solution treatment and aging; (c) change in {1 1 3} interplanar spacing of matrix with aging time at the different aging temperatures (1250–1550 °C), as estimated from the shifts in the α-Al_2O_3 peak positions in the as aged samples with respect to the peak positions of the as-sintered A10F solid solution.

that the interplanar spacing decreases with time at all the three aging temperatures. However, as compared to the lower temperatures (1250 and 1350 °C), the activity is significantly higher at the higher temperatures (1450 and 1550 °C). Furthermore, the plots indicate that the precipitation reaction seems to reach completion after ∼15 h at 1450 °C and only ∼10 h at 1550 °C, with no further diminution of dissolved Fe^{3+} on further increase in aging time. By contrast, at the lower temperatures the interplanar spacing continues to decrease with increasing duration up to 50 h, with no indication of the precipitation reaction reaching completion even after aging for such an extended duration.

3.2. Microstructural development

3.2.1. As-sintered microstructures

Fig. 2 presents representative back scattered scanning electron micrographs (BSE) of polished and thermally etched surfaces of pure Al_2O_3 (a) and A10F (b). The absence of significant residual porosity, as observed from the micrographs of the sintered samples, was confirmed by the density measurements which showed that all the samples were densified to >98% of their theoretical density. It is evident from Fig. 2 that the presence of dissolved Fe considerably alters the size and morphologies of the Al_2O_3 grains. For pure Al_2O_3 the grains are fairly equiaxed in shape, without any observable abnormal or anisotropic grain growth (Fig. 2a), with the grain sizes varying between 2 and 4 μm. In contrast, the Fe-containing samples show microstructures characterised by the presence of a few large elongated grains in a matrix of finer equiaxed grains. The equiaxed grains possess sizes ranging between 1 and 3 μm, while some of the elongated grains have lengths varying between 5 and 8 μm and widths between 2 and 3 μm (Fig. 2b). No evidence of any secondary phase can be detected on the BSE image of the as-sintered (solution treated) Fe_2O_3 containing Al_2O_3 (Fig. 2b). The absence of secondary phase either along the matrix grain boundaries or within the matrix grains was also confirmed by TEM investigation (Fig. 2c). In accordance with the XRD results these observations further confirm that the sintering (solution treatment) step results in complete dissolution of 10 wt.% Fe_2O_3 in Al_2O_3. The distribution of the various elements (Al, Fe, O) present in the microstructure of as-sintered A10F has been revealed by X-ray elemental mapping (Fig. 3). The important observation is that Fe is distributed uniformly throughout the microstructure. Within the limits of X-ray mapping, no preferential segregation of dissolved Fe along the matrix grain boundaries can be observed in the as-sintered microstructure, which is in agreement with an earlier report by Tartaj and Messing.[21]

3.2.2. Bulk microstructural development on aging

Backscattered SEM (BSE-SEM) images obtained from near the cores of the samples, aged at the various temperatures for different durations in the reducing atmosphere, are shown in Figs. 4–6. The presence and average sizes of the inter and intragranular second phase particles corresponding to the different aging schedules, as estimated from the BSE-SEM images, are also reported in Table 1. The presence of a secondary phase

Table 1
Effect of aging temperatures (1250–1550 °C) and times (0–50 h) on the distribution and size of second phase particles ($FeAl_2O_4$) precipitated during reduction of A10F solid solutions in reducing atmosphere ($N_2 + 4\%\ H_2$).

Aging time (h)	Reduction aging temperature: 1250 °C		Reduction aging temperature: 1350 °C		Reduction aging temperature: 1450 °C		Reduction aging temperature: 1550 °C	
	Intergranular particles size (µm)	Intragranular particles size (nm)	Intergranular particles size (µm)	Intragranular particles size (nm)	Intergranular particles size (µm)	Intragranular particles size (nm)	Intergranular particles size (µm)	Intragranular particles size (nm)
0	0.8 ± 0.4	Not present	0.8 ± 0.7	Not present	1.1 ± 0.6	Not present	2.9 ± 0.6	Not present
5	–	Not present	1.1 ± 0.2	Not present	1.5 ± 0.8	Not present	5.4 ± 0.8	79 ± 17
10	1.2 ± 0.5	Not present	1.5 ± 0.4	Not present	1.7 ± 0.5	71 ± 27	Not measured due to excessive pull out	88 ± 19
15	–	Not present	1.8 ± 0.2	Not present	1.9 ± 0.5	104 ± 38	Not measured due to excessive pull out	119 ± 47
20	1.6 ± 0.3	Not present	2.2 ± 0.5	Not present	2.2 ± 0.3	127 ± 34	Not measured due to excessive pull out	153 ± 29
50	2.4 ± 0.7	Not present	5.1 ± 0.9	97 ± 21	Not measured due to network formation	321 ± 63	Not measured due to excessive pull out	521 ± 56

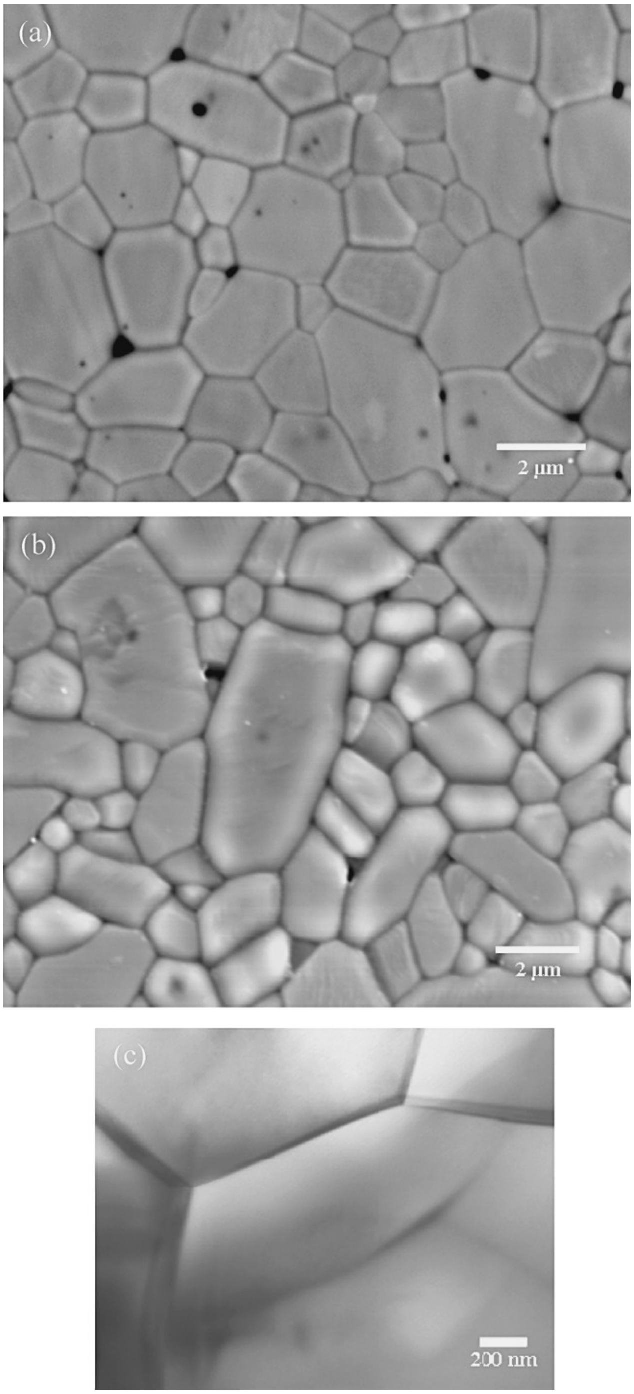

Fig. 2. Back scattered scanning electron micrographs (BSE-SEM) obtained from polished and thermally etched surfaces of as-sintered (a) pure Al_2O_3 and (b) A10F. (c) TEM image corresponding to as-sintered (solution treated) A10F, confirming the absence of any secondary phase along the matrix grain boundaries or within the grains.

(brighter contrast) is clearly revealed in the BSE-SEM images corresponding to the ground and polished surfaces of the samples aged for the maximum duration of 50 h at the lower temperatures of 1250 and 1350 °C (Fig. 4a and b). However this secondary phase is present only as coarse, micro-scale particles mainly along the boundaries and at the triple point corners of the matrix grains. The precipitation of second phase particles within the

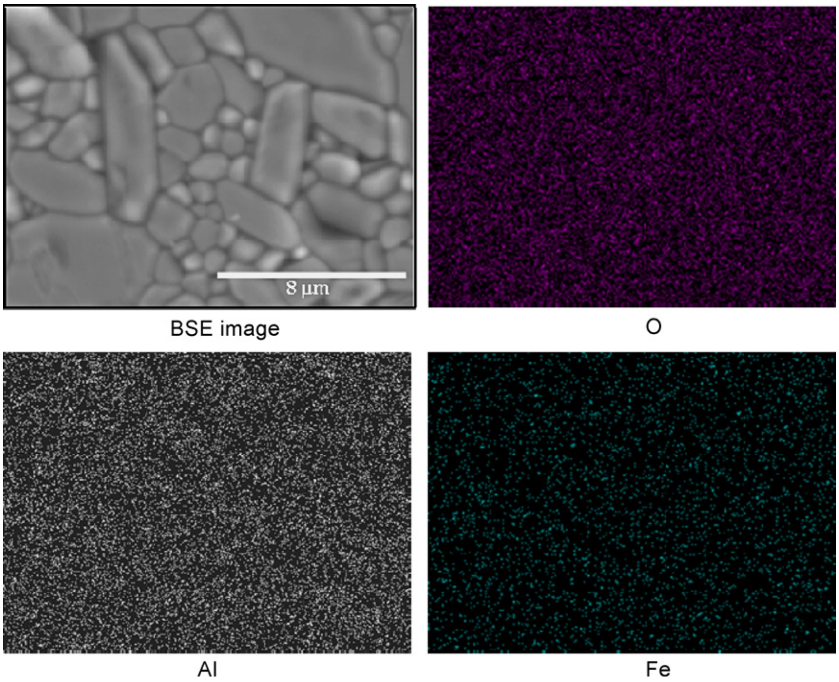

Fig. 3. X-ray elemental mapping, showing the uniform distribution of the various elements (Al, O, Fe) present on the polished thermally etched surface of as-sintered A10F.

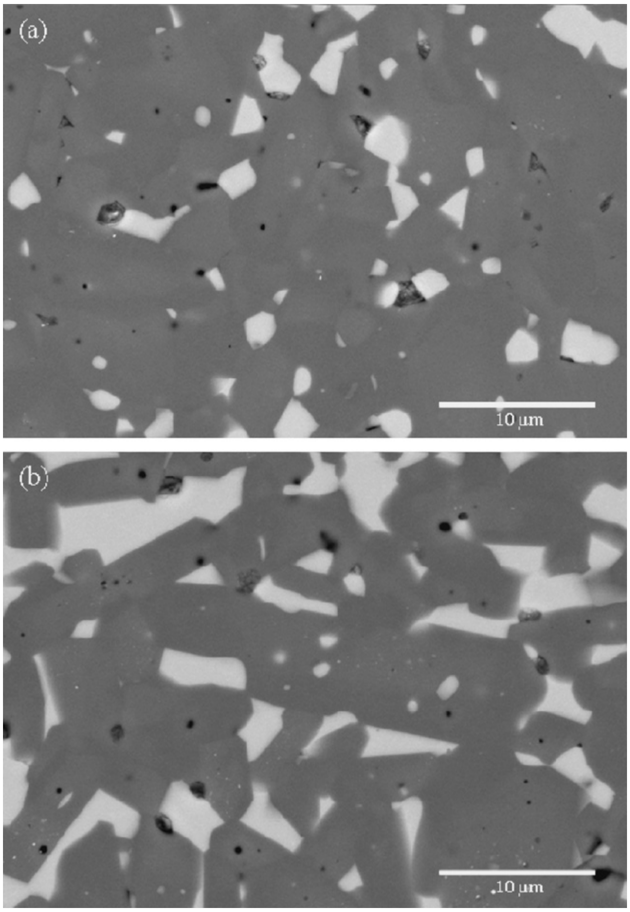

Fig. 4. Back scattered SEM images obtained from ground and polished surfaces (sample core) of A10F, aged for 50 h in reducing atmosphere ($N_2 + 4\% \ H_2$) at the lower aging temperatures of (a) 1250 °C and (b) 1350 °C.

matrix grains seems to be difficult at these lower temperatures, even on holding for an extended period of time (50 h).

The bulk microstructures after reduction aging at 1450 °C for different times are presented in Fig. 5. Again, only micro-scale grain boundary particles appear during the initial stages (0–5 h) of aging (see Fig. 5a). However, on continued aging for durations of 10 h or more at 1450 °C, extremely fine 'nano-sized' second phase particles (~70 nm) precipitated within the matrix grains, along with the continuing presence of the coarser intergranular particles (Fig. 5b). On further aging (up to 20 h) modest coarsening of both the inter- and intragranular particles (Fig. 5c) occurred. On aging for the extended duration of 50 h at 1450 °C significant microstructural coarsening occurred, with the intragranular particles growing to submicron size (~0.3 μm) along with the formation of a nearly interconnected network of intergranular spinel phase (Fig. 5d). EDS spectra confirms the presence of more Fe in the second phase particles with respect to the matrix (Fig. 5). The intragranular particles retained a nano- or submicron size for all the aging schedules studied (see Table 1).

Excessive coarsening of the intergranular $FeAl_2O_4$ particles, as observed for the samples aged for 50 h at 1450 °C (Fig. 5), also occurred during aging at the highest investigated aging temperature of 1550 °C even for much shorter durations (~10 h) (Table 1 and Fig. 6). Precipitate free zones, which usually form due to the depletion from near the grain boundary regions of the solute atoms which join the heterogeneously nucleated intergranular precipitate particles, can also be observed near the grain boundary particles in the BSE micrographs of the as aged samples (Figs. 5a and b and 6). Another interesting observation was that the composites containing a very coarse and interconnected network of intergranular $FeAl_2O_4$ particles suffered considerable pull out of these particles during metallographic polishing,

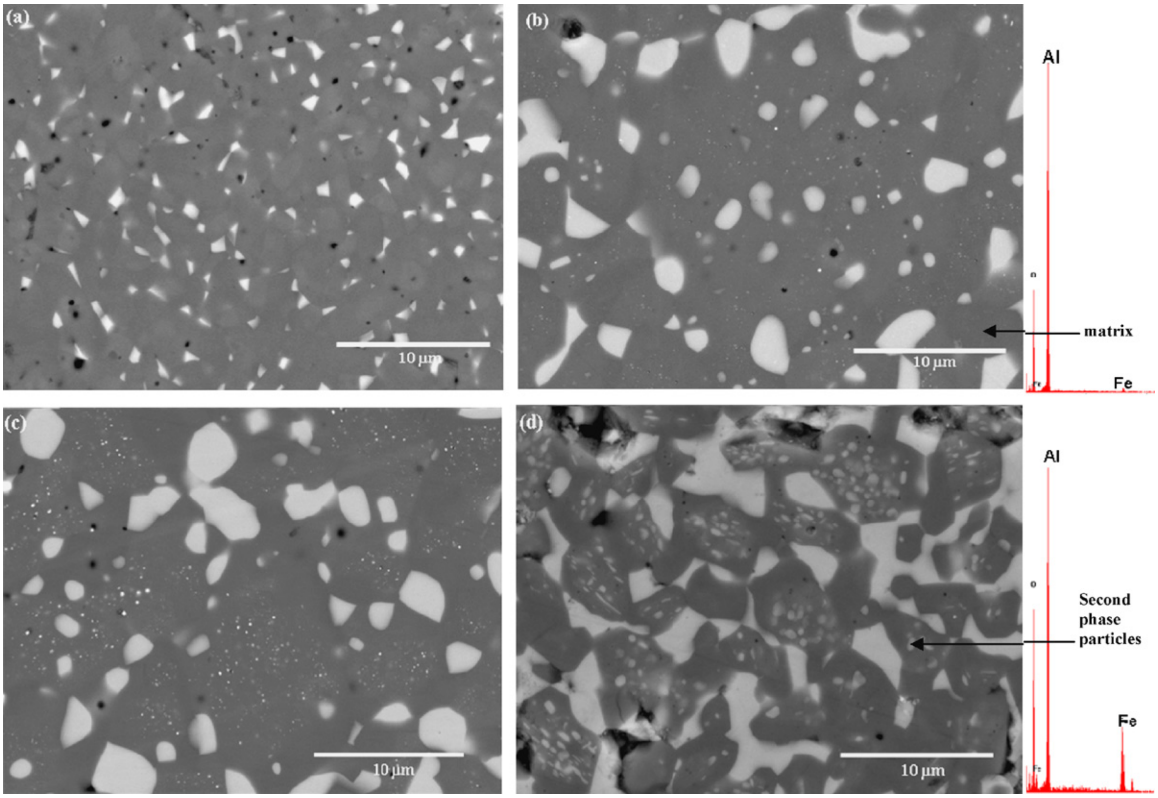

Fig. 5. Back scattered SEM micrographs obtained from the as ground and polished surfaces (sample core) of A10F, aged in reducing atmosphere ($N_2 + 4\% \ H_2$) at 1450 °C for (a) 0 h; (b) 10 h; (c) 20 h; (d) 50 h. EDX spectra obtained from the matrix and the second phase particles are also presented.

which leads to a poorer surface finish for the ‘over-aged’ samples. This is in complete contrast to the samples developed by aging for shorter duration ($\leq$20 h) at 1450 °C, which can be polished to a better surface finish and more easily than monolithic Al_2O_3, as is the case for Al_2O_3–SiC nanocomposites.[7,22,23]

The percentage of the volume occupied by the secondary phase in the Al_2O_3–$FeAl_2O_4$ ‘nanocomposites’, as determined from BSE-SEM images via point counting, are plotted as functions of aging durations for the different aging temperatures in Fig. 7. It can be observed that, as compared to the higher temperatures of 1450 and 1550 °C, a significantly lower amount of secondary phase particles can be produced at the lower temperatures, reaching a maximum of only ~6% at 1250 °C and ~14% at 1350 °C even on aging for the extended duration of 50 h. By

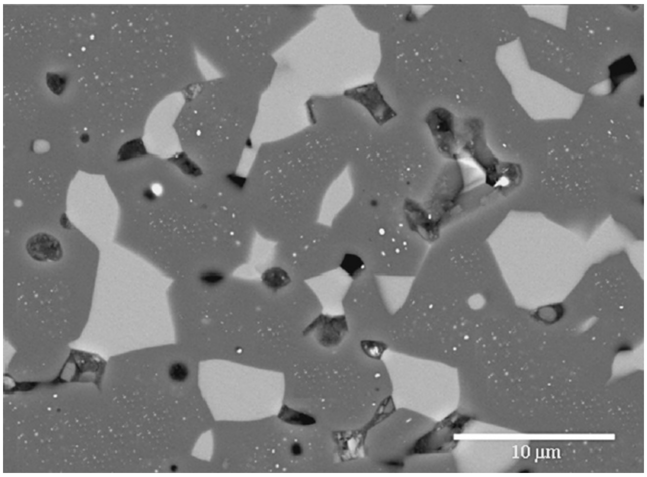

Fig. 6. Back scattered SEM micrographs obtained from the as ground and polished surfaces (sample core) of A10F, aged in reducing atmosphere ($N_2 + 4\% \ H_2$) at 1550 °C for 10 h. Note the occurrence of significant microstructural coarsening, resulting in the presence of extremely coarse and nearly interconnected network of intergranular secondary phase, after just 10 h of aging at the highest investigated temperature of 1550 °C.

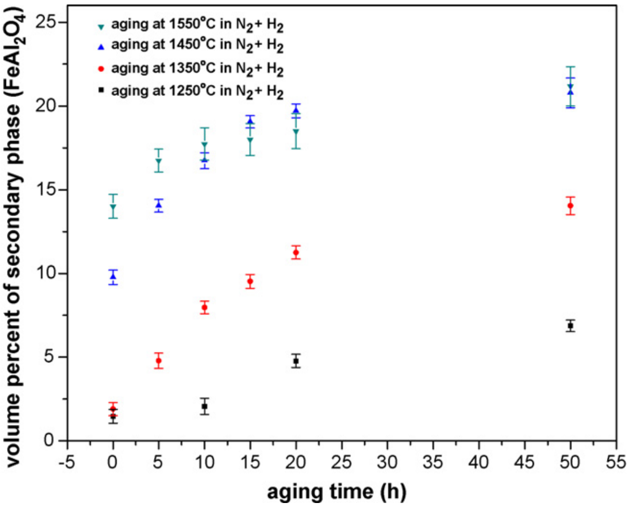

Fig. 7. Variation of volume percent of the secondary phase ($FeAl_2O_4$) formed as a function of aging time (0–50 h) at the different investigated aging temperatures (1250–1550 °C). The volume fractions have been estimated via point counting method on back scattered SEM images.

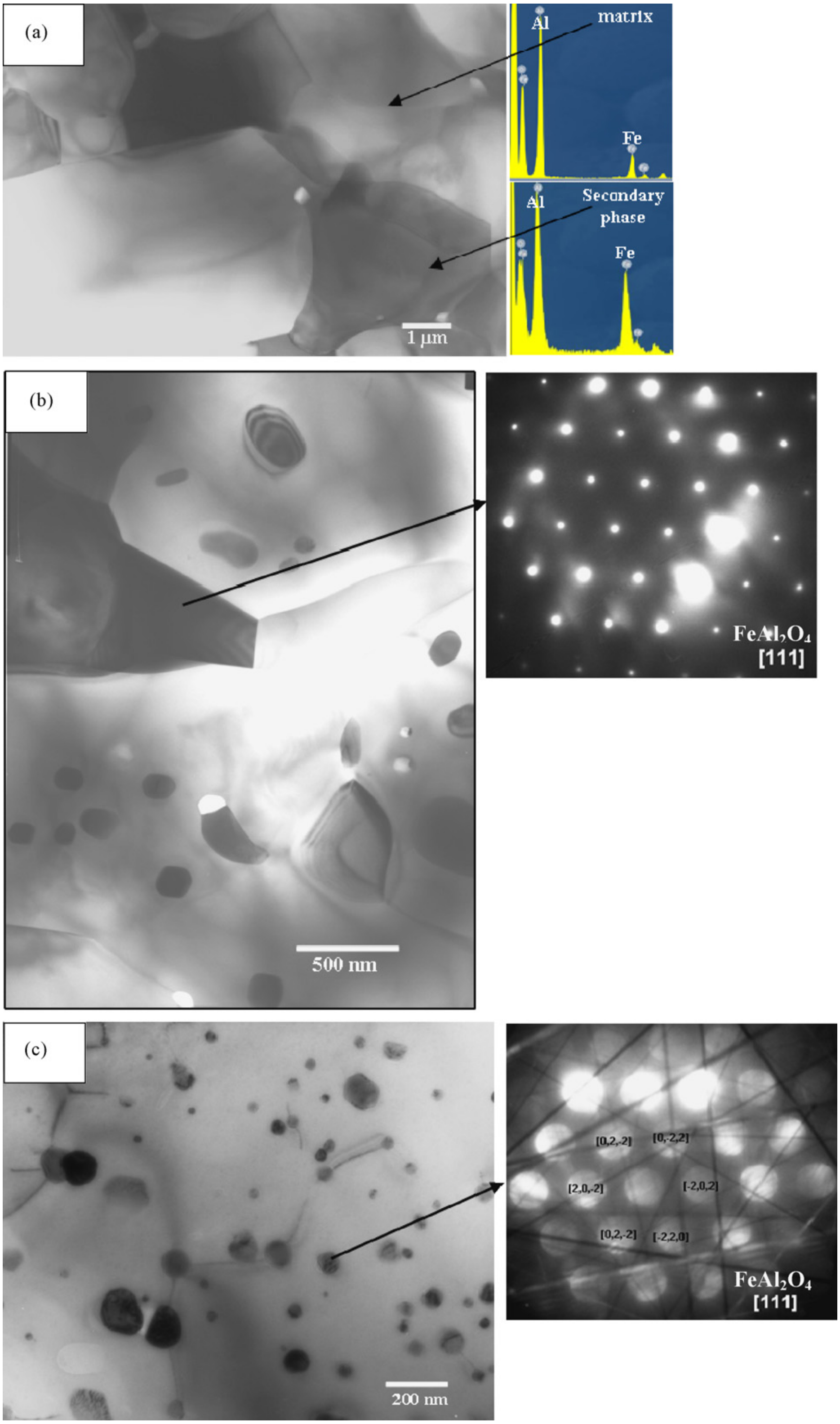

Fig. 8. Bright field TEM images corresponding to (a) as aged A10F sample (1350 °C; 50 h; $N_2 + H_2$ atmosphere), revealing the presence of only coarse Fe-rich (see EDS spectra) secondary phase particles along the matrix grain boundaries; (b) as aged A10F (1450 °C; 20 h; $N_2 + H_2$ atmosphere), revealing the presence of coarser second phase particles along the matrix grain boundaries, along with nano-sized particles within the matrix grains; (c) closer look at higher magnification within a matrix grain in as aged A10F (1450 °C; 10 h; $N_2 + H_2$ atmosphere) shows the distribution of intragranular nano-sized secondary phase particles. Selected area diffraction patterns obtained from the coarser intergranular particles (b), as well as convergent beam diffraction patterns obtained from the nano-sized intragranular particles (c), can be indexed with respect to $FeAl_2O_4$.

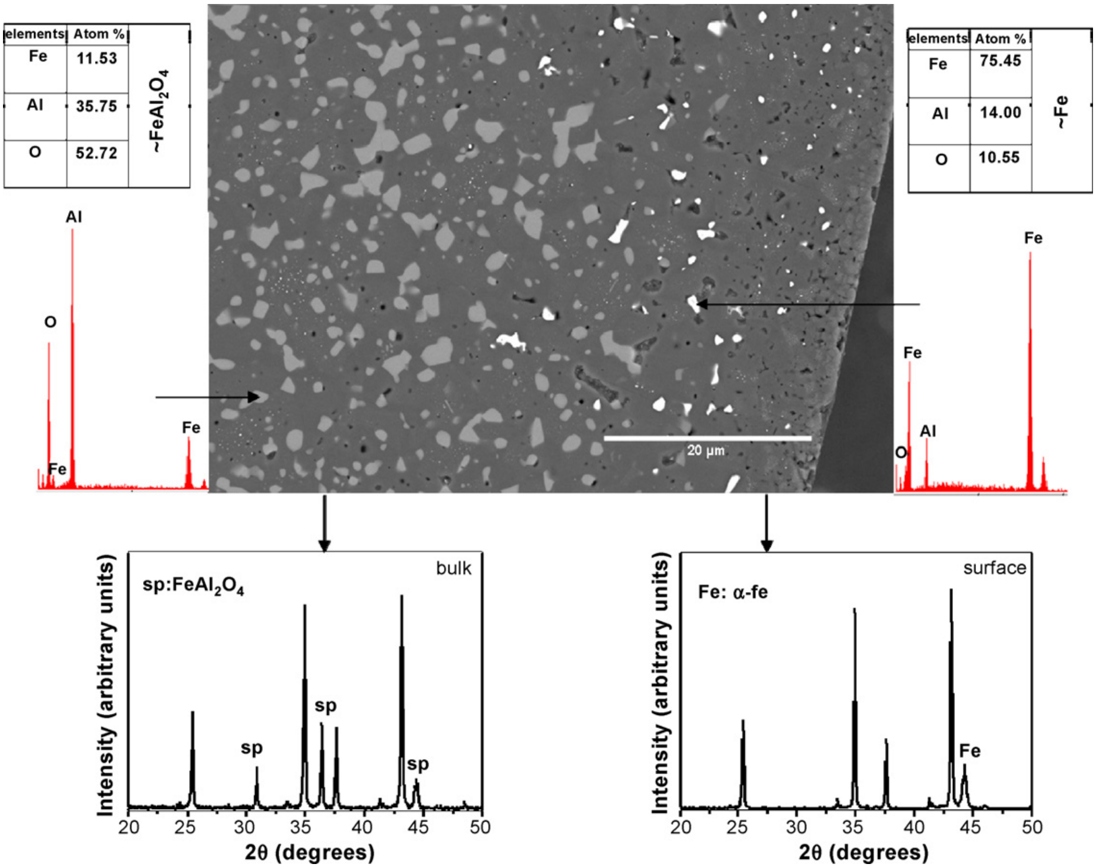

Fig. 9. BSE image of cross-sectional view of as aged (1450 °C; 20 h; $N_2 + H_2$) A10F sample, showing the presence of Fe as the secondary phase (brighter contrast) near the surface, as opposed to $FeAl_2O_4$ in the bulk. EDX spectra obtained from the respective secondary phases, along with XRD patterns collected from the surface (before grinding) and the bulk (after grinding/polishing), confirm the presence of α-Fe at the surface of the aged samples.

contrast, a volume percent as high as 19–20% is achievable on aging at 1450 °C for a period of 20 h or more. It must be mentioned here that point counting may provide an underestimate of the second phase content because some of the very tiny particles may not be detected during the estimation and some of the coarser intergranular particles may be lost due to pull out during polishing (especially for the 1550 °C aged composites).

The distribution of the second phase particles can be seen more clearly from the corresponding bright field transmission electron micrographs (TEM) (Fig. 8). In agreement with the SEM observations, the presence of only coarse intergranular second phase particles can be seen in the microstructures corresponding to the samples aged at the lower temperature of 1350 °C (Fig. 8a). By contrast, the presence of nano-sized secondary phase particles within the matrix grains, along with coarser intergranular particles can be observed in the TEM images corresponding to the sample aged at 1450 °C for optimum durations (Fig. 8b and c). Elementary analysis via EDS shows that the second phase particles are Fe-rich relative to the bulk matrix (Fig. 8a). Furthermore, selected area diffraction patterns (SADP) obtained from the micron-sized intergranular particles, as well as the convergent beam diffraction patterns (CBED) recorded from the nano-sized intragranular particles confirms that the second phase particles present in the bulk microstructure of the as aged ‘nanocomposites’ are $FeAl_2O_4$ (Fig. 8b and c). Another interesting observation that can be made from the TEM images is the absence of strain contrast around the second phase particles for all the aging schedules studied.

3.2.3. Effect of reduction aging on external surfaces

The cross-sections of the as aged samples were observed in SEM after cutting along a diameter of the pellets, followed by metallographic polishing. A cross-section from a sample aged at 1450 °C for 20 h in $N_2 + H_2$ is presented in Fig. 9. There exists a zone near the surface with a thickness of ~20 μm where the second phase particles appear brighter in contrast than the particles present below such zone and all through the bulk of the sample. The depth from the surface of such Fe-containing zone increases with aging time at a given temperature, reaching a maximum observed thickness of ~100 μm on aging at 1550 °C for the extended duration of 50 h. Analysis of the EDS spectra collected from such brighter particles, along with comparison of spectra collected from the more prevalent less bright particles present in the core of the sample, suggests that the second phase particles present along the surface layer are metallic Fe. Representative EDS spectra corresponding to the two different types of particle, along with quantitative analysis, are presented in Fig. 9. Furthermore, XRD patterns recorded from the surface before grinding/polishing confirm the absence of $FeAl_2O_4$ and the presence of metallic α-Fe as the second phase at the surface (see Fig. 9). Formation of similar layered Al_2O_3-based composite microstructures containing $FeAl_2O_4$ as the secondary phase

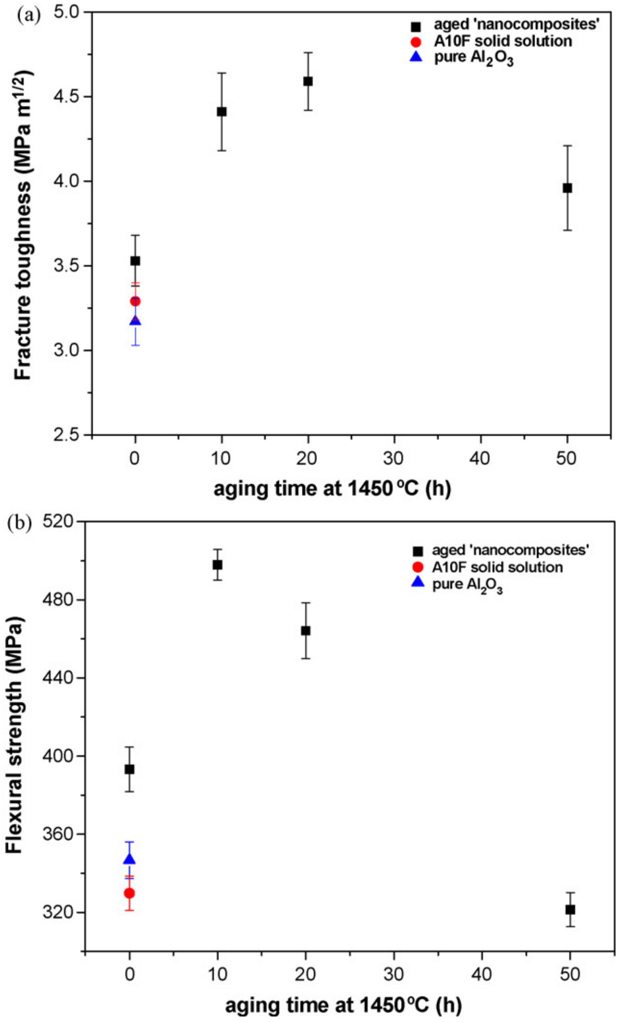

Fig. 10. Room temperature (a) fracture toughness, as measured by SEVNB and (b) flexural strength, as determined from four-point bending, for pure Al_2O_3, A10F solid solution and the Al_2O_3–$FeAl_2O_4$ composites/nanocomposites developed after reduction aging of A10F solid solution for different durations (0–50 h) at 1450 °C.

in the bulk and a surface layer containing metallic Fe has also been previously observed during spark plasma sintering in vacuum of Al_2O_3–7 mol% Fe_2O_3 powders.[24] However in the cited work,[24] the amount, size and distribution of the secondary phase particles were not studied.

3.3. Mechanical properties and fracture surfaces

The room temperature fracture toughness and flexural strength of the Al_2O_3–$FeAl_2O_4$ micro/nanocomposites, developed on reduction aging at 1450 °C are shown in Fig. 10. The surfaces subjected to tensile stresses during the four-point bending experiments were ground and polished sufficiently to remove the Fe-containing surface layers for all the specimens. The incorporation of Fe^{3+} to make a solid solution (A10F) did not result in any significant change in the fracture toughness and strength with respect to pure Al_2O_3. Aging the solid solution at 1450 °C for “0 h”, producing only grain boundary precipitates, gave only a modest improvement in fracture toughness and strength. Aging for longer durations, however, resulted in considerable improvement in the mechanical properties, with the ‘hybrid micro/nanocomposites’ developed on aging for optimum durations of 10–20 h at 1450 °C exhibiting ~40% improvement in fracture toughness and ~50% improvement in flexural strength with respect to monolithic Al_2O_3. However, significant degradation of the properties, in particularly the flexural strength, resulted on further aging for the extended duration of 50 h.

SEM images corresponding to the fractured surfaces obtained during toughness testing of as-sintered monolithic Al_2O_3, A10F solid solution and the nanocomposites developed via reduction aging are presented in Fig. 11. It can be observed that monolithic Al_2O_3 (Fig. 11a), A10F solid solution (Fig. 11b), as well as the composite developed on reduction aging for 0 h (Fig. 11c) exhibited the classical almost completely intergranular mode of fracture. By contrast, the fracture mode changed to almost purely transgranular fracture on aging for 10 h or more at 1450 °C (Fig. 11d and e). Another observation that can be made from the higher magnification BSE image obtained from the fractured surface of the nanocomposite aged for 20 h (Fig. 11f), is that although the intragranular nano-sized particles appear to remain intact within the matrix upon fracture, the coarser intergranular particles seem to have fallen out during the fracture process.

The nanocomposites developed on reduction aging at 1450 °C for 0–20 h possessed hardnesses between 18 and 19 GPa, which are comparable with that of pure Al_2O_3 (~20 GPa) and slightly improved with respect to that of A10F solid solution (~17 GPa). However, the hardness of the ‘composite’ aged for 50 h (~17 GPa) appears to be slightly less than that of pure Al_2O_3 and the ‘nanocomposites’ developed by aging for shorter duration. Another important observation that can be made from SEM images of the Vickers indents is that although monolithic Al_2O_3 exhibits pronounced radial cracking (Fig. 12a), the lengths of the cracks are less for the ‘nanocomposites’, as would be expected from their higher toughness values (Fig. 12b).

4. Discussion

4.1. Progress of precipitation reaction

Comparison of Figs. 1c and 7 reveals that the decrease in interplanar spacings of the matrix with aging duration agrees well with the increase in volume fraction of the second phase particles. Such agreement implies that the change in interplanar spacing is not affected by strains in the lattice caused due to coherency of the second phase particles with the matrix. Furthermore, TEM observations show the absence of any strain contrast around the particles. Such observations suggest that the equilibrium $FeAl_2O_4$ particles formed during the reduction aging treatment are semicoherent or incoherent with the matrix.

Assuming that all the Fe comes out of solid solution as $FeAl_2O_4$, the maximum volume percent of $FeAl_2O_4$ that can be theoretically produced by reduction aging of the A10F solid solutions is 21%. As can be inferred from the investigations of the progress of the precipitation reaction via both the methods and the microstructural developments, the kinetics are signif-

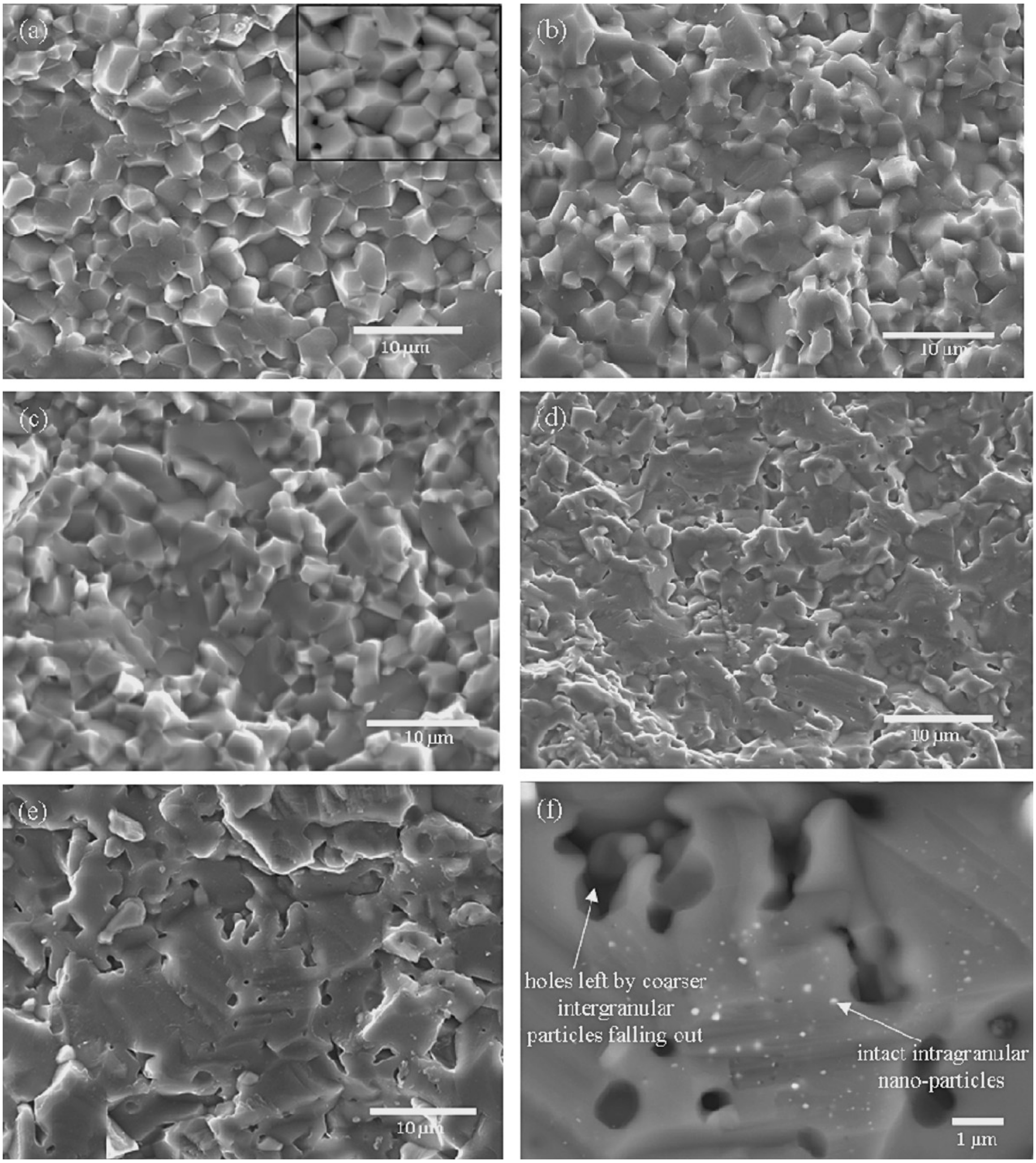

Fig. 11. SEM images of fractured surfaces obtained during Fracture toughness testing (SEVNB) of (a) monolithic Al_2O_3; (b) as-sintered A10F solid solution; Al_2O_3–$FeAl_2O_4$ nanocomposite developed by reduction aging of A10F solid solution at 1450 °C for (c) 0 h; (d) 10 h; (e) 20 h; and (f) higher magnification BSE-SEM image of fractured surface of Al_2O_3–$FeAl_2O_4$ nanocomposite (aged; 1450 °C; 20 h).

icantly slower at temperatures below 1450 °C, which neither allows the reaction to go to completion (maximum $FeAl_2O_4$ content of ∼6 vol.% at 1250 °C and ∼14 vol.% at 1350 °C), nor leads to the formation of the intragranular particles even after aging for the extended duration of 50 h. However, the precipitation reaction goes to completion after 10–15 h during aging at the higher temperatures of 1450 °C and 1550 °C ($FeAl_2O_4$ content ∼20 vol.%), with nano-sized intragranular particles appearing after ∼10 h. Considering that nucleation of particles is easier at grain boundaries and that grain boundary diffusion coefficients are higher than bulk diffusion coefficients it is not surprising that the incubation period is higher and growth rate lower for precipitation of intragranular particles compared with the particles along the matrix grain boundaries. It must be noted that to the best of the authors' knowledge the development of oxide–oxide nanocomposites, containing such high volume fractions of second phase particles (up to ∼20 vol.%), via aging has not been reported previously. Furthermore, development of dense Al_2O_3–SiC nanocomposites via pressureless sintering has been achieved only for nanocomposites containing a maximum of 5 vol.% SiC particles, and then at much higher temperatures.[12]

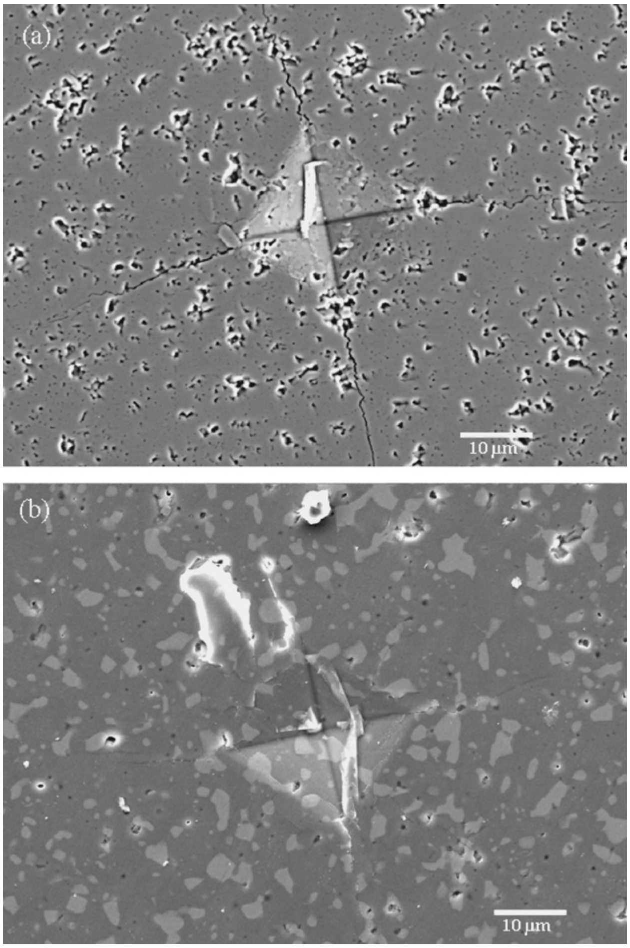

Fig. 12. Vickers indents, as obtained with a maximum load of 2 kg on ground and polished surfaces of (a) pure Al_2O_3 (b) Al_2O_3–$FeAl_2O_4$ nanocomposite developed on aging of A10F solid solution at 1450 °C for 20 h in reducing atmosphere.

4.2. *Overall chemical reactions responsible for $FeAl_2O_4$ and Fe phase evolutions*

The present processing scheme, which involves aging in the presence of H_2 as the reducing agent, leads to changes in the chemical composition of the starting materials (solid solution of Fe_2O_3 in Al_2O_3) to result in the formation of new phases ($FeAl_2O_4$ and Fe). With regard to the formation of metallic Fe at the surface layer, it has been observed that the depth from the surface of the Fe-containing zone increased with aging time at a given temperature. These surface layers contained hardly any $FeAl_2O_4$ particles. This suggests that the as precipitated $FeAl_2O_4$ particles get further reduced to metallic Fe progressively from the surface during continued aging. Such partially transformed $FeAl_2O_4$ particles (to Fe), present near the interface of the Fe-containing surface layer and the bulk, can also be observed on BSE micrographs obtained from the cross-sections (Fig. 13a and b). Furthermore, TEM observations of foils developed from near the surface regions of the as aged composites revealed that some portions of some of the second phase particles possess different contrasts, with respect to the other regions of the same particles, when tilted at various orientations with respect to the incident beam (Fig. 13c and d). CBED patterns obtained from these portions can be indexed in terms of α-Fe (Fig. 13d). It is believed that the presence of metallic Fe in a portion of the second phase particles, as observed from the SEM as well as TEM images, is due to $FeAl_2O_4$ getting transformed to Fe.

The following chemical reactions are proposed to account for the overall phase evolutions. The initial composition corresponding to the solid solution of 10 wt.% Fe_2O_3 in Al_2O_3 can be represented by $Al_{1.868}Fe_{0.132}O_3$. Considering that $FeAl_2O_4$ is formed as the second phase throughout the bulk of the samples on reduction aging, the following reaction:

$$Al_{1.868}Fe_{0.132}O_3 + 0.066H_2 \rightarrow 0.132FeAl_2O_4 + 0.802Al_2O_3 + 0.066H_2O(g) \quad (3)$$

is supposed to make the major contribution. At the surfaces the $FeAl_2O_4$ gets further reduced to metallic Fe. The following reaction is believed to account for this additional reduction step;

$$FeAl_2O_4 + H_2 \rightarrow Fe + Al_2O_3 + H_2O(g) \quad (4)$$

It can be observed that both the reactions lead to the removal of O^{2-} which should result in mass loss during aging. The theoretical mass loss accompanying reaction (3) is estimated to be ∼0.998%, while reaction (4) should result in an additional mass loss of ∼1.996%. The overall mass loss after reduction aging for different time–temperature schedules will depend on the extent of both the reactions taking place for the respective schedules. The extent of the overall reaction (3) after aging for different durations at 1450 °C has been estimated based on the relative change in interplanar spacing at the respective aging times with respect to that after 20 h, when the precipitation reaction is believed to have reached equilibrium (see Fig. 1c). The depth of the zones from the surface corresponding to the formation of metallic Fe (due to reaction (4)) has been noted for the different aging schedules, which allows the estimation of the mass loss resulting from the additional occurrence of reaction (4) at such surface layers. The net mass losses due to occurrence of reaction (3) throughout the samples, along with the additional contribution from reaction (4) at the surface, have been estimated for all the aging durations at the optimum aging temperature of 1450 °C. As presented in Fig. 14, such estimations have been found to correlate well with the experimentally measured mass losses for the different aging durations, supporting the validity of Eqs. (3) and (4).

The metallic Fe at the surface should not preclude the use of these ceramic alloys in wear resistant applications, as this very thin layer would very soon be removed. In any case we believe that the formation of Fe can be avoided completely by the use of a less reducing atmosphere for the aging treatments (e.g. with a lower H_2/H_2O ratio or a different reducing agent). Further investigations are underway to explore such possibilities.

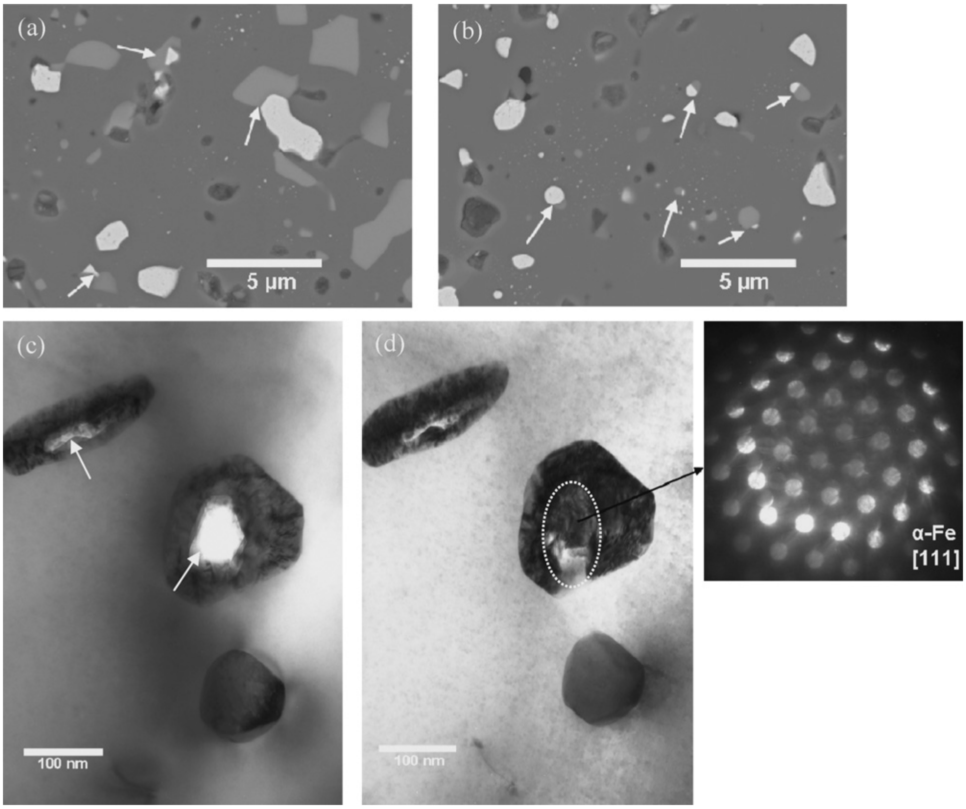

Fig. 13. (a) and (b) BSE-SEM images showing the presence of $FeAl_2O_4$ particles being partially transformed to Fe (brighter portion). Such particles are indicated with arrows. (c) TEM image, as obtained with foil prepared from near the surface of aged A10F (1450 °C; 20 h; $N_2 + H_2$), showing the presence of a different phase (having brighter contrast) at some portion the secondary phase particles (indicated with arrows). (d) CBED pattern obtained from the small region corresponding to the different phase can be indexed in terms of α-Fe.

4.3. *Correlation between microstructural development, fracture mode and mechanical properties*

Critical assessment of the observed variation of the fracture properties with reduction aging duration points towards some correlations between the aging duration, microstructural development (volume fraction, size and distribution of the second phase particles), fracture mode and the strength/fracture toughness for the as developed composites (Figs. 5, 10 and 11). It has been observed that neither the incorporation of Fe^{3+} in solid solution, nor the limited precipitation of micron-sized $FeAl_2O_4$ particles along the matrix grain boundaries and triple point corners (on aging at 1450 °C for 0 h) changed the fracture mode from intergranular to transgranular. At the same time, such solution treatment and aging treatment did not lead to any obvious improvement in the fracture properties. By contrast, aging for longer periods (≥10 h) resulted in the precipitation of nano-sized second phase particles within the matrix grains, and concomitantly led to significant improvement in the fracture toughness and strength. This precipitation of nano-sized second phase particles within the matrix grains also coincided with the change in fracture mode to purely transgranular for the nanocomposites. These observations suggest that change in fracture mode had some effect on the improvement of fracture toughness and strength, as measured for the nanocomposites. It must be mentioned here that Hansson and co-workers[25] have estimated that a change in fracture mode from intergranular to transgranular fracture in alumina can lead to an increase in the fracture toughness of 30–50%, which is sufficient to account for at least the majority of the 40% toughness increase found here.

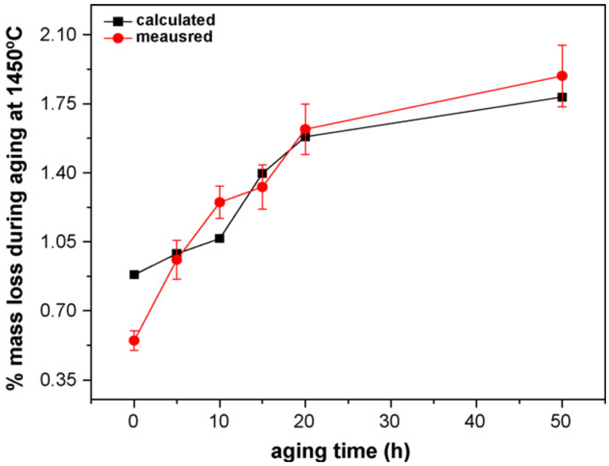

Fig. 14. Mass loss (experimentally measured and theoretically estimated) as a function of aging time (0–50 h) during reduction aging of A10F solid solutions at 1450 °C.

However, on continued aging for 50 h, the fracture toughness of the composites deteriorated and was accompanied by a significant reduction in the flexural strength. We suggest that this is the result of the formation of the very coarse and nearly interconnected particles seen in Fig. 5d. These were observed to fall out during metallographic polishing (Figs. 5d and 6) and fracture (Fig. 11f) and are therefore consistent with a reduction in resistance to fracture and an increase in critical flaw size.

5. Conclusions

The present report illustrates that a novel processing route, based on solution treatment and aging in reducing atmosphere, can successfully lead to alumina-based oxide–oxide hybrid micro/nanoceramic composites using pressureless sintering. More specifically:

(a) Pressureless sintering at 1450 °C for 5 h in air can lead to the development of a single phase homogeneous solid solution of 10 wt.% Fe_2O_3 in Al_2O_3 (solution treatment).
(b) Subsequent heat treatments in reducing atmosphere (N_2–4% H_2 forming gas mixture) at various temperatures between 1250 and 1550 °C for different durations up to 50 h resulted in the precipitation of $FeAl_2O_4$ throughout the bulk of the samples (reduction aging).
(c) Reduction aging at the optimised temperature of 1450 °C for 10–20 h resulted in the formation of intragranular, nano-sized particles of $FeAl_2O_4$ in addition to micron-sized particles along the matrix grain boundaries. However, significant coarsening of the second phase particles occurred on aging for an elongated time period of ~50 h or at the highest investigated temperature of 1550 °C.
(d) Within a certain depth from the surface $FeAl_2O_4$ gets further reduced to metallic Fe during reduction aging. The thickness of this surface layer increases with aging up to ~100 μm on aging at 1550 °C for 50 h.
(e) The 'hybrid nano/microcomposite', developed on aging for optimum duration (between 10 and 20 h at 1450 °C), possessed improved fracture toughness (by ~40%) and flexural strength (by ~50%) with respect to pure Al_2O_3, accompanied by a change in fracture mode to transgranular fracture.

Acknowledgement

The authors would like to thank Vanessa de Castro, Department of Materials, Oxford University, for her help with analysis of TEM images.

References

1. Mukhopadhyay A, Basu B. Consolidation–microstructure–properties of bulk nanoceramics and ceramic nanocomposites: a review. *Intl Mater Rev* 2007;**52**(4):1–32.
2. Niihara K. New design concept of structural ceramics. *J Ceram Soc Jpn* 1991;**99**:974–82.
3. Limpichaipanit A, Todd RI. The relationship between microstructure, fracture and abrasive wear in Al_2O_3/SiC nanocomposites and microcomposites containing 5 and 10% SiC. *J Eur Ceram Soc* 2009;**29**:2841–8.
4. Ortiz Merino JL, Todd RI. Relationship between wear rate, surface pull-out and microstructure during abrasive wear of alumina and alumina/SiC nanocomposites. *Acta Mater* 2005;**53**:3345–57.
5. Biswas K, Mukhopadhyay A, Basu B, Chattopadhyay K. Densification and Microstructural development in Spark Plasma Sintered WC–6 wt.% ZrO_2 Nanocomposites. *J Mater Res* 2007;**22**(6):1491–501.
6. Wang Y, Fujimoto T, Maruyama H, Koga K. Precipitation of magnesium aluminum spinel from alumina-matrix solid solution: I. Fundamental concept and precipitation behavior. *J Am Ceram Soc* 2000;**83**(4):933–6.
7. Mukhopadhyay A. Tribological properties and processing challenges of bulk structural ceramic nanomaterials. *Tribology—Materials, Surfaces & Interfaces* 2008;**2**(3):169–84.
8. Walker CN, Borsa CE, Todd RI, Davidge RW, Brook RJ. Fabrication, characterisation and properties of alumina matrix nanocomposites. *Br Ceram Proc* 1994;**53**:249–64.
9. Borsa CE, Jiao S, Todd RI, Brook RJ. Processing and properties of Al_2O_3/SiC nanocomposites. *J Microsc* 1995;**177**:305–12.
10. Zhang Y, Wang L, Jiang W, Chen L, Bai G. Microstructure and properties of Al_2O_3–TiC nanocomposites fabricated by spark plasma sintering from high-energy ball milled reactants. *J Eur Ceram Soc* 2006;**26**:3393–7.
11. Liu H, Huang C, Wang J, Teng X. Fabrication and mechanical properties of $Al_2O_3/Ti(C_{0.7}N_{0.3})$ nanocomposites. *Mater Res Bull* 2006;**41**:1215–24.
12. Shapiro IP, Todd RI, Titchmarsh JM, Roberts SG. Effects of Y_2O_3 additives and powder purity on the densification and grain boundary composition of Al_2O_3/SiC nanocomposites. *J Eur Ceram Soc* 2009;**29**(9):1613–24.
13. Hsu SE, Kobes W, Fine ME. Strengthening of sapphire by precipitates containing titanium. *J Am Ceram Soc* 1967;**50**(3):149–51.
14. Phillips DS, Heuer AH, Mitchell TE. Precipitation in star sapphire I. Identification of the precipitate. *Phil Mag A* 1980;**42**(3):385–404.
15. Langensiepen RA, Tressler RE, Howell PR. A preliminary study of precipitation in Ti^{4+}-doped polycrystalline alumina. *J Mater Sci* 1983;**18**:2771–6.
16. Lee HY, Paek YK, Lee BK, Kang SJL. Discontinuous dissolution of iron aluminate spinel in the Al_2O_3–Fe_2O_3 system. *J Am Ceram Soc* 1995;**78**(8):2149–52.
17. Coble RL. Sintering crystalline solids. II. Experimental test of diffusion models in powder compacts. *J Appl Phys* 1961;**32**(5):793–9.
18. Cullity BD. *Elements of X-ray Diffraction*. 2nd ed. London, UK: Addison-Wesley Publishing Company Inc.; 1978. pp. 350–382.
19. Mizuno M, Okuda H. VAMAS round robin on fracture toughness of silicon nitride. *J Am Ceram Soc* 1995;**78**:1793–801.
20. Atkinson KJW, Grimes RW, Levy MR, Coull ZL, English T. Accommodation of impurities in α-Al_2O_3, α-Cr_2O_3 and α-Fe_2O_3. *J Eur Ceram Soc* 2003;**23**:3059–70.
21. Tartaj J, Messing GL. Anisotropic grain growth in α-Fe_2O_3 doped alumina. *J Eur Ceram Soc* 1997;**17**:719–25.
22. Winn AJ, Todd RI. Microstructural requirements for alumina-SiC nanocomposites. *Br Ceram Trans* 1999;**98**:219–24.
23. Kara H, Roberts SG. Polishing behavior and surface quality of alumina and alumina/silicon carbide nanocomposites. *J Am Ceram Soc* 2000;**83**(5):1219–25.
24. Santanach JG, Estournes C, Weibel A, Peigney A, Chevallier G, Laurent C. Spark plasma sintering as a reactive sintering tool for the preparation of surface-tailored Fe–$FeAl_2O_4$–Al_2O_3 nanocomposites. *Scripta Mater* 2009;**60**:195–8.
25. Hansson T, Warren R, Wasen J. Fracture toughness anisotropy and toughening mechanisms of a hot-pressed alumina reinforced with silicon carbide whiskers. *J Am Ceram Soc* 1993;**76**(4):841–8.